nature communications

Article

https://doi.org/10.1038/s41467-025-57732-7

Filamentation activates bacterial Avs5 antiviral protein

Received: 4 October 2024

Accepted: 27 February 2025

Published online: 11 March 2025

Check for updates

Yiqun Wang[1], Yuqing Tian[1], Xu Yang[1], Feng Yu[1] & Jianting Zheng[1,2]

Bacterial antiviral STANDs (Avs) are evolutionarily related to the nucleotide-binding oligomerization domain (NOD)-like receptors widely distributed in immune systems across animals and plants. EfAvs5, a type 5 Avs from *Escherichia fergusonii*, contains an N-terminal SIR2 effector domain, a NOD, and a C-terminal sensor domain, conferring protection against diverse phage invasions. Despite the established roles of SIR2 and STAND in prokaryotic and eukaryotic immunity, the mechanism underlying their collaboration remains unclear. Here we present cryo-EM structures of EfAvs5 filaments, elucidating the mechanisms of dimerization, filamentation, filament bundling, ATP binding, and NAD^+ hydrolysis, all of which are crucial for anti-phage defense. The SIR2 and NOD domains engage in intra- and inter-dimer interaction to form an individual filament, while the outward C-terminal sensor domains contribute to bundle formation. Filamentation potentially stabilizes the dimeric SIR2 configuration, thereby activating the NADase activity of EfAvs5. Furthermore, we identify the nucleotide kinase gp1.7 of phage T7 as an activator of EfAvs5, demonstrating its ability to induce filamentation and NADase activity. Together, we uncover the filament assembly of Avs5 as a unique mechanism to switch enzyme activities and perform anti-phage defenses.

Bacteria are in constant conflict with bacteriophages and develop diverse anti-phage defense systems of varying complexity[1–3]. The signal transduction ATPases with numerous domains (STANDs) of P-loop NTPases, such as animal inflammasomes and plant resistosomes, recognize pathogens or host-derived signals, triggering inflammatory responses or apoptotic processes through oligomerization[4–6]. This represents a conserved immune strategy in eukaryotes. Recently, this mechanism has also been discovered in the innate immunity of bacteria, known as antiviral STANDs (Avs)[3]. Avs proteins have a characteristic tripartite domain architecture: a central NTPase (alternatively called nucleotide-binding oligomerization domain, NOD); an extended C-terminal sensor with superstructure-forming repeats; and a variable N-terminal effector typically involved in cell death. Previous studies have revealed that Avs1-3 and Avs4 are activated by the phage terminases and portals, respectively, leading to the formation of tetramers that activate their N-terminal nucleases for antiviral defense[7].

Avs type 5 (Avs5) contains an N-terminal sirtuin (SIR2) effector and an unusual short C-terminal sensor domain, also termed SIR2-STAND[3]. SIR2-mediated nicotinamide adenine dinucleotide hydrolase (NADase) activity represents a critical element in anti-phage immunity, triggering abortive infections via NAD^+ degradation and halting phage propagation, as exemplified by pAgo, Thoeris, DSR2, and the SIR2-HerA system[8–11]. In the Thoeris system, the signaling molecule 1″–3′ gcADPR activates ThsA, which subsequently forms filaments and depletes NAD^+, ultimately triggering cell death and thereby preventing the spread of phage infection[12]. Another defense system DSR2 tetramerizes to form a supramolecular complex that specifically recognizes phage tail tube proteins and leads to cellular NAD^+ depletion[13]. Despite reports on SIR2 and STAND roles in prokaryotic and eukaryotic immunity, the mechanisms underlying their synergistic interactions remain uncharacterized.

Here, we present a biochemical and structural analysis of *Escherichia fergusonii* Avs5 (EfAvs5), unveiling a unique mechanism of

[1]State Key Laboratory of Microbial Metabolism, School of Life Sciences and Biotechnology, Shanghai Jiao Tong University, Shanghai, China. [2]Joint International Research Laboratory of Metabolic & Developmental Sciences, Shanghai Jiao Tong University, Shanghai, China. e-mail: jtzheng@sjtu.edu.cn

assembly-mediated activation of EfAvs5. EfAvs5 proteins form active filaments via SIR2 and NOD self-association, with sensor-mediated filament bundling enhancing their organization, allowing NAD^+ depletion during phage infection. The inactive NOD of EfAvs5 requires ATP binding for its defensive role, whereas ATP impedes its NADase activity. We also find that phage nucleotide kinase gp1.7 of phage T7, which is not previously associated with bacterial defense system, activates EfAvs5 to from filament bundles and perform NADase activity.

Results

EfAvs5 consumes NAD^+ to confer defense

Avs5 system is widely distributed across Gram-negative phyla, especially *Pseudomonadota* (Supplementary Fig. 1). To define the molecular mechanism of Avs5 defense systems, we investigated an Avs5 protein from *E. fergusonii* (EfAvs5) (Fig. 1a), which is reported to defend against diverse *Escherichia coli*, *Salmonella* and *Klebsiella pneumoniae* phages[14]. As expected, *E. coli* cells expressing EfAvs5 are resistant to phage T7. The C terminal sensor domain is supposed to detect the phage invasion, while the SIR2 domain is suggested to be the effector depleting NAD^+. A single amino acid substitution at the SIR2 active site (N141A) was sufficient to abolish phage defense of EfAvs5. Similarly, a point mutation disrupting the NOD active site (K379A in Walker A or D426A in Walker B) or deleting the C-terminal sensor domain also abolished defense (Fig. 1a).

E. coli cells expressing EfAvs5 continued growing when infected by phage T7 at low (0.2) or medium (2) multiplicity of infection (MOI) compared to cells expressing N141A mutant or lacking EfAvs5 (Fig. 1b). We measured the colony formation of cells infected by phage T7 relative to uninfected cells and found that EfAvs5 increased cell survival after the first infection cycle (about 20 minutes) (Fig. 1c). Live/dead staining revealed that the majority of cells expressing EfAvs5 were viable when infected by phage T7 at an MOI of 2 (Supplementary Fig. 2). Further analysis showed that phages amplified rapidly in the cells lacking EfAvs5, but not in the cells expressing EfAvs5 (Fig. 1d). To investigate the NADase activity during immunity, we detected the cellular NAD^+ content following infection by phage T7. Compared to cells lacking EfAvs5, the NAD^+ concentration in the cells expressing EfAvs5 declined rapidly after the first infection cycle, but began to rise in the second infection cycle (Fig. 1e). These results suggest that EfAvs5 consumes NAD^+ to effectively prevent phage amplification and leads to the population-level protection. However, EfAvs5 obviously does not act through a canonical abortive infection (abi) mechanism that induces cell death or dormancy upon infection. According to a recently proposed categorization that decouples the defense mechanism from the fate of the host[15], EfAvs5 can be classified as "survival by targeting cellular components", like DSR1 system[10].

Architecture of EfAvs5 filament assembly

Freshly purified EfAvs5 exists as a soluble monomer (Supplementary Fig. 3). Cryo-EM imaging of the monomeric EfAvs5 revealed small particles. We tried to resolve the structure but only obtained two-dimensional (2D) classes in poor resolution, possibly due to the flexibility (Supplementary Fig. 4). However, the purified EfAvs5 (approximately 20 μM) becomes cloudy after two weeks of storage at 4 °C or −80°C. Visualization of the sample by negative staining EM revealed the formation of filament bundles (Fig. 2a). Since previous studies show that the activated SIR2 or Toll/interleukin-1 receptor (TIR) can

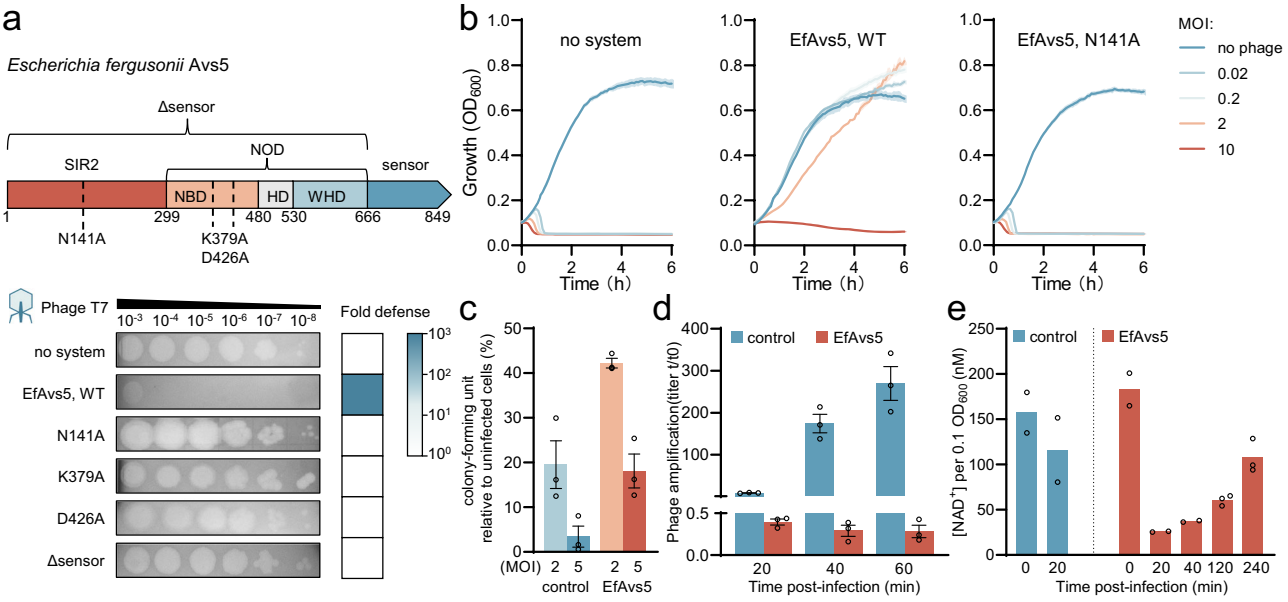

Fig. 1 | EfAvs5 consumes NAD^+ to confer defense. a Domain organization of the EfAvs5 protein from *Escherichia fergusonii* and efficiency of plaquing of phages infecting *E. coli* expressing EfAvs5 or an empty vector. Data are representative images of $n = 3$ biological replicates. The mutations used are indicated below the domain organization. NBD, nucleotide-binding domain; HD, helical domain; WHD, wing-helical domain; NOD, nucleotide-binding oligomerization domain. **b** Infection time courses for liquid cultures of *E. coli*, with EfAvs5, EfAvs5 N141A or empty vector, infected at different multiplicities of infection (MOI) of phage T7. Data represent the mean of three replicates, and shaded regions represent the standard error of the mean (SEM). **c** Colony-forming units of *E. coli* cells expressing either the EfAvs5 or empty vector as a control infected at an MOI of 2 and 5 with T7 for 20 minutes. Data represent the mean of three replicates, and error bars represent the SEM, with individual data points overlaid. **d** Titer of phage T7 propagated on *E. coli* cells expressing either the EfAvs5 or empty vector as a control infected at an MOI of 0.1 with T7. Data represent the titer of T7 measured in plaque-forming units (PFU)/mL after indicated time from initial infection, divided by the original phage titer prior to infection. Data represent the mean of three replicates, and error bars represent the SEM, with individual data points overlaid. **e** Measurement of NAD^+ concentration in *E. coli* expressing EfAvs5 or empty vector as a control at the indicated time points after infection with phage T7 at an MOI of 2, normalized to an OD_{600} of 0.1. The control group underwent near-complete lysis after 20 minutes of infection, precluding the quantification of NAD^+ content. Data with the avs5 system at 120 and 240 minutes represent three biological replicates; others represent two replicates; all individual data points are shown. Source data are provided as a Source Data file.

https://doi.org/10.1038/s41467-025-57732-7

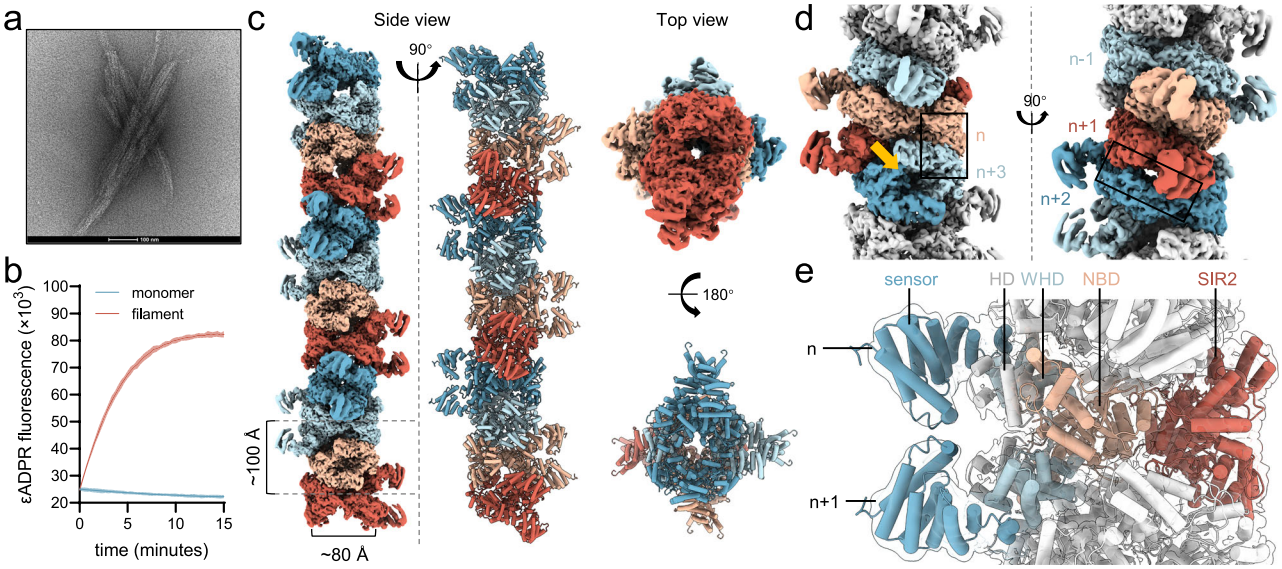

Fig. 2 | Cryo-EM structure of the EfAvs5 filament. a Negative-stain micrograph images of EfAvs5, representative of >5 fields of view with similar results. The scale bar represents 100 nm. **b** EfAvs5's NADase activity is activated by filamentation. After the addition of ε-NAD$^+$, total fluorescence was measured over time. Data represent the mean of three replicates, and shaded regions represent the SEM. **c** Top and side views of the density map and the atomic model of EfAvs5 filament. **d** Detailed view of EfAvs5 filament to show the subunit interfaces. Two interfaces are indicated with boxes, and the NAD$^+$ active site is indicated with an orange arrow. **e** The core of EfAvs5 filament is composed of the SIR2 domain and the NOD. Source data are provided as a Source Data file.

assemble into helical filaments in Thoeris defense system, TIR-STING and TIR-SAVED effector, respectively[12,16,17], we assayed the NADase activity of EfAvs5. The freshly purified EfAvs5 was inactive, but the EfAvs5 filament bundles displayed robust NADase activity (Fig. 2b). To analyze the effect of concentration on EfAvs5 filamentation, EfAvs5 proteins of different concentrations were prepared and stored at −80°C. As shown in Supplementary Fig. 5, samples with concentrations greater than or equal to 5 μM began to show significant turbidity after 7 days. Dynamic light scattering (DLS) analysis showed a significant increase in particle radius, and NADase activity also increased with storage time.

We determined a cryo-electron microscopy (cryo-EM) structure of a EfAvs5 filament. The final cryo-EM map was reconstructed using a total of 228,053 single particles and refined to a nominal resolution of 3.4 Å, with approximately 2.8 Å at the center and approximately 6.8 Å at the peripheral sensor lobes (Fig. 2c, Supplementary Fig. 6 and Supplementary Table 1). The model contains eight EfAvs5 molecules assembled into a helical filament, and extra densities suggest unlimited entries of both ends. The repeating building block of the filament is EfAvs5 dimer with a C_2 symmetry, which is arranged into a regular helical structure with a helical twist of 84.531° and a helical rise of 48.600 Å (Fig. 2c). The filament is held together by 2 sets of inter-subunit interactions, one between subunit n and n + 3 and the other between subunit n + 1 and n + 2 (Fig. 2d). An EfAvs5 subunit folds into five domains: a SIR2 effector domain, a core NOD, which comprises the nucleotide-binding domain (NBD), helical domain (HD) and wing-helical domain (WHD), and a C-terminal sensor domain (Fig. 1a and Fig. 2e). The core of the helix is composed of the SIR2 and the NOD, whereas the C-terminal sensor is pointing away and not involved in the helical contacts (Fig. 2e).

SIR2- and NOD-dependent filamentation

The EfAvs5 dimer buries an interface of 2329.2 Å^2 (Fig. 3a). Contacts are observed between the WHD of one subunit and the NBD of the other subunit, revealing a dimeric pattern distinct from previously characterized active STAND ATPases, which primarily dimerize through NBD-NBD and WHD-WHD interactions (Supplementary Fig. 7). Three salt bridges are involved in the dimerization mediated by the WHD and the NBD (Fig. 3b). The dimeric interface is expanded by additional hydrogen bonds between its N-terminal SIR2 domains (Fig. 3c). To probe the importance of dimer formation in EfAvs5 function, we introduced mutations at the dimeric interface. K241A, T262A, H362A, and K461A mutants were purified from *E. coli* by the same protocol as wild-type EfAvs5 (Supplementary Fig. 8). These mutants didn't become cloudy after two weeks of storage, and NADase activity was undetectable (Supplementary Fig. 9). In contrast to wild-type EfAvs5, these mutants are not toxic to *E. coli* when induced by IPTG. As expected, these substitutions abolished the antiviral defense of EfAvs5 (Fig. 3d).

Both SIR2 and NOD are involved in dimer-dimer interactions, resulting in two spirals: one dominated by SIR2 and the other by NOD (Fig. 4a, b and e). The SIR2 domain of EfAvs5 exhibits a typical two-domain fold (Fig. 4d), resembling that of DSR2 (PDB ID: 8WYB, rmsd of 1.160 Å for 74 aligned Cα atoms) and ThsA (PDB ID: 8BTO, rmsd of 1.247 Å for 84 aligned Cα atoms)[12,13], except for a longer α3 creating a broader substrate channel (Supplementary Fig. 10). The large domain (LD) has a Rossmann-fold core that is conserved among all the SIR2 proteins, while the small domain (SD) lacks the three-stranded zinc-binding motif compared to human Sirt5[18].

The interface between SIR2 dimers is non-parallel to the helical axis (Fig. 4a), burying ~1200 Å^2 of surface area (Fig. 4b). SIR2 α4, α10 and α12 helices contribute to the intra-dimer interactions (Fig. 3c), whereas the loop connecting β3 and β4 forms polar interactions and hydrogen bonds with the loop between β4 and α9 of the adjacent SIR2, thereby constituting the inter-dimer interactions and facilitating the assembly of EfAvs5 filaments (Fig. 4c). Interestingly, despite the similarity of the structure, the oligomerization mechanism of EfAvs5-SIR2 is different from SIR2-HerA, ThsA and DSR2 (Supplementary Fig. 11). Similar to the intra-dimer interaction, the inter-dimer interactions of NOD also mainly include the NBD-WHD contacts, but adopt a different mechanism (Fig. 4e). The NBD interface of the n + 1 molecule is predominantly negatively charged (I303, E307, E404), complementing the positively charged interface of WHD domain of n + 2 molecule (K552, H622, K623) (Fig. 4f, g). To probe the role of the filament formation in EfAvs5 activity, we generated D164A or R185A mutation in the interface between n and n + 3 subunits, and I303A/E307A, E404A/K552A or H622A/K623A double mutation in the interface between n + 1 and

https://doi.org/10.1038/s41467-025-57732-7

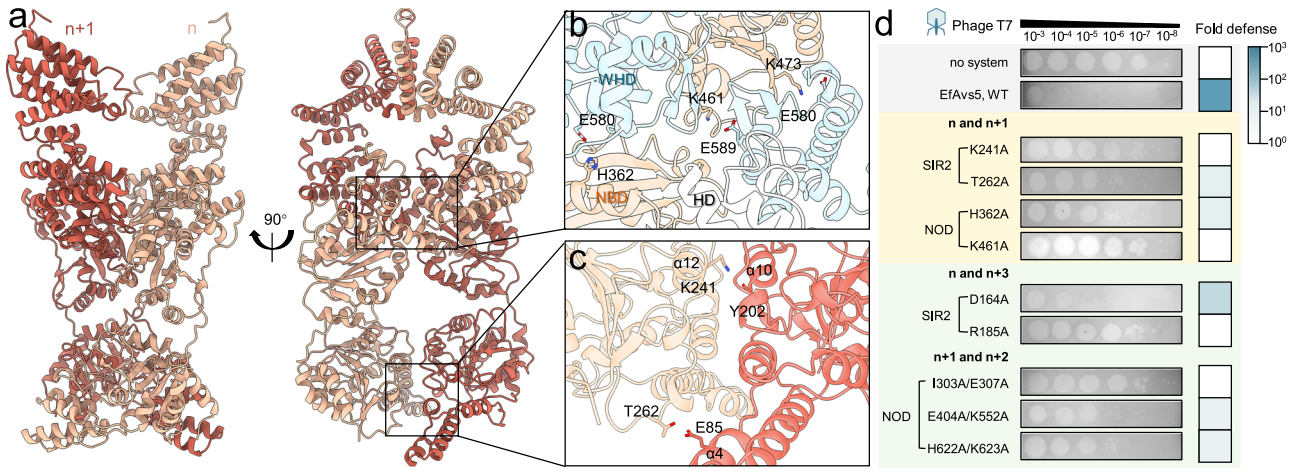

Fig. 3 | Dimerization of EfAvs5. a The structure of the EfAvs5 dimer. **b** Details of the NOD-based dimeric interfaces. **c** Details of the SIR2-based dimeric interfaces. **d** Phage plaque assay of *E. coli* expressing EfAvs5 variants with mutations at the interfaces. The yellow background highlights the intra-dimer interactions, while the green background indicates the inter-dimer interactions. Data are representative images of $n = 3$ biological replicates. Source data are provided as a Source Data file.

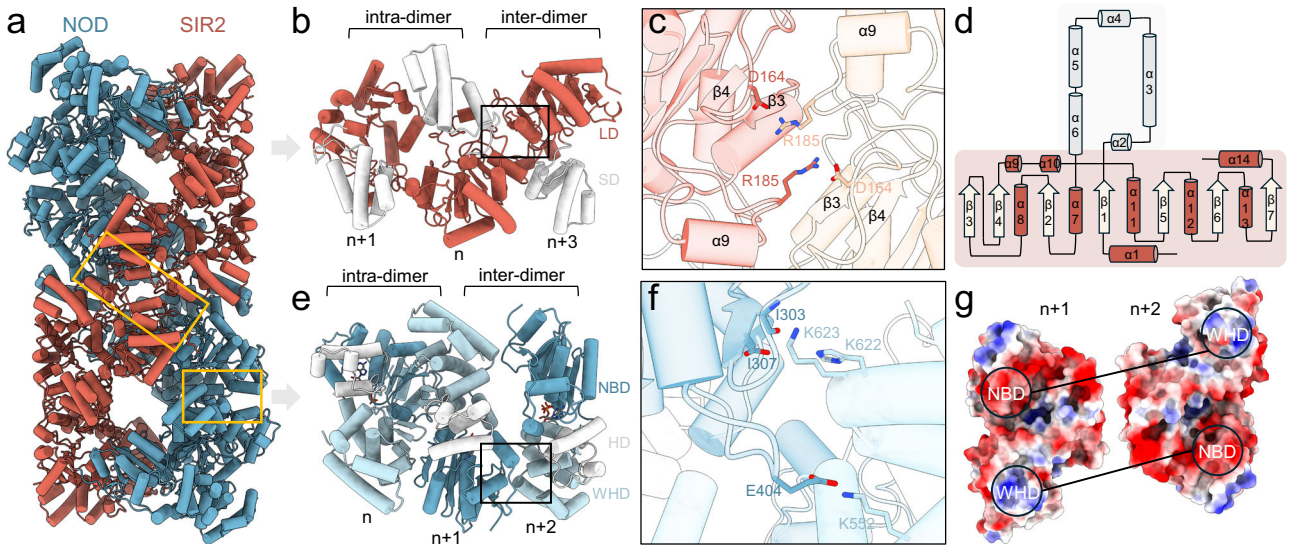

Fig. 4 | SIR2- and NOD-dependent filamentation. a Two spirals dominated by NOD (blue) and SIR2 domains (red), respectively. The C-terminal domains of EfAvs5 are not displayed. The inter-dimer interactions are indicated by orange boxes. **b** The intra-dimer and inter-dimer interface of SIR2 domain of the n + 1, n, n + 3 subunits. LD, large domain; SD, small domain. **c** Detailed inter-dimer interface of SIR2 domain. The n, n + 3 subunits of EfAvs5 were colored red and orange, respectively. **d** SIR2 topology diagrams of EfAvs5. The small domain is shaded grey, and the large domain is shaded red. **e** The intra-dimer and inter-dimer interface of NOD domain of the n, n + 1, n + 2 subunits. **f** Detailed inter-dimer interface of NOD domain. The NBD of n + 1 subunit, and the WHD of n + 2 subunit of EfAvs5 were colored dark and light blue, respectively. **g** The electrostatic potential inter-dimer interface of two adjacent NOD domains.

n + 2 subunits. We purified these mutants (Supplementary Fig. 8), but didn't observe turbidity or NADase activity after two weeks of storage (Supplementary Fig. 9). Among all these mutants, only D164A demonstrated weak cytotoxicity when induced by IPTG (Supplementary Fig. 9c). Additionally, all these mutations abolished or weakened antiviral defense of EfAvs5 (Fig. 3d).

NADase catalytic pocket

The SIR2 of EfAvs5 adopts a similar conformation observed in the activated SIR2 of ThsA (Fig. 5a). In the case of ThsA and DSR2, the position of the loop above the active pocket either blocks or enables NAD^+ access to the active site, thus control the NADase activity of SIR2[12,19]. However, in the EfAvs5, the longer α3 pulls this loop far away from the active pocket (Fig. 5a and Supplementary Fig. 10), indicating a different mechanism to modulate NADase activity. In the predicted model of EfAvs5-NAD^+, the residues A41, T140, N141, Y142, N180, Y202, S233 of the pocket interact with NAD^+, creating a suitable conformation for the reaction (Fig. 5b). These residues are highly conserved in the bacterial SIR2 proteins, except for residue S233 and the substitution of Asn by His at residue 180 in EfAvs5 (Supplementary Fig. 12). To investigate the role of these amino acids in NAD^+ hydrolysis, the corresponding mutants were purified (Supplementary Fig. 8). With the exception of N180A and Y202A, other mutants were well expressed and exhibited high turbidity after two weeks of storage (Supplementary Fig. 9a). While none of them exhibited NADase activity in vitro (Supplementary Fig. 9b), the induction of T140A and S233A demonstrated cytotoxicity (Supplementary Fig. 9c).

ATP inhibits the NADase activity of EfAvs5

The NOD of EfAvs5 is an AAA^+ ATPase, belonging to a novel STAND NTPase 3 family found in bacterial conflict systems and metazoan TRADD-N associated counter-invader proteins[20]. The structural

https://doi.org/10.1038/s41467-025-57732-7

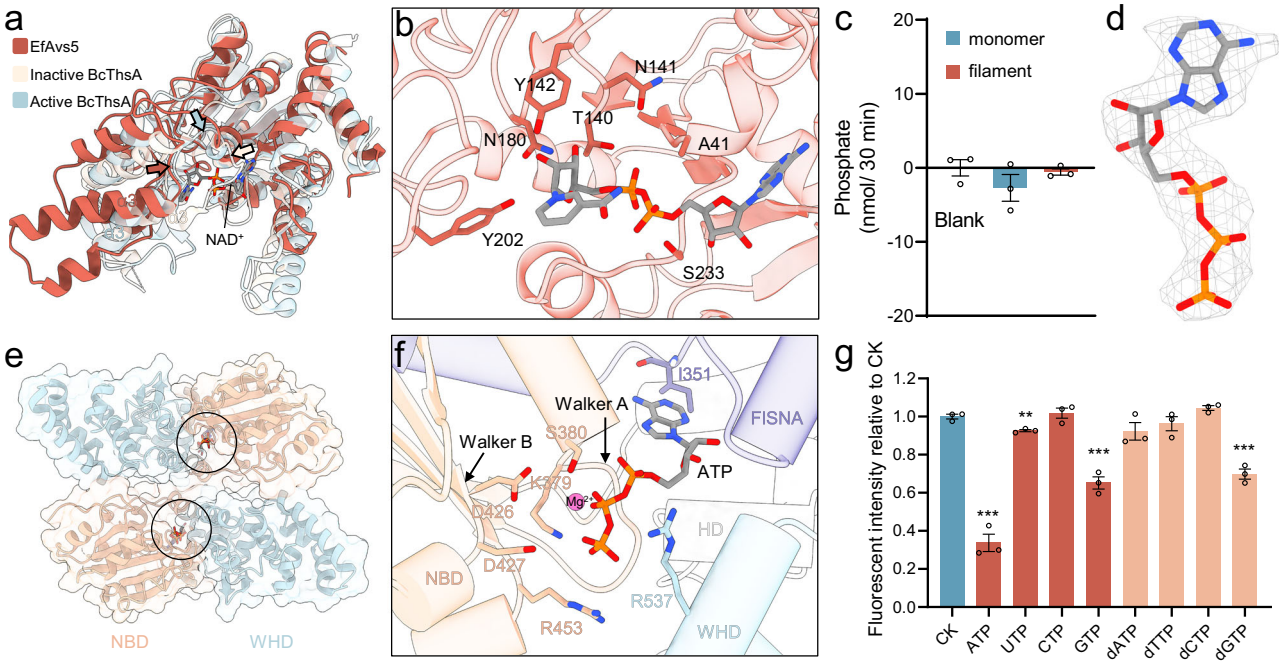

Fig. 5 | The NAD⁺ hydrolyzing pocket and ATP binding pocket of EfAvs5. **a** Overlay of SIR2 domain (red) of EfAvs5 with the inactive (6LHX, light orange) and activated (8BTO, light blue) *Bacillus cereus* ThsA (BcThsA) SIR2 domains. NAD⁺ from the activated ThsA (1ICI) is shown. The loops above the NAD⁺ pocket of EfAvs5 and ThsA SIR2 are indicated by arrows colored as in the color scheme. **b** Residues of EfAvs5 interacting with NAD⁺ molecule highlighted in sticks in the predicted EfAvs5-NAD⁺ binding model. **c** ATPase activity assay of the monomer or the filament EfAvs5. Data represent the mean of three replicates, and error bars represent the SEM, with individual data points overlaid. *P*-values are compared to the blank group by two-sided Student's *t*-test, and exact values are provided in the Source Data File. **d** Cryo-EM map of ATP. **e** The binding pocket of ATP in the NOD dimer. **f** Residues of EfAvs5 coordinating ATP molecule highlighted in sticks. The highly conserved Walker A motif and Walker B motif were indicated by arrows. FISNA, fish-specific NACHT-associated domain. **g** Effects of NTPs and dNTPs (5 mM) on the NADase activity of EfAvs5, showing the ratio of fluorescence changes observed within 15 minutes compared to the control group (CK), which had no NTPs/dNTPs added. Data represent the mean of three biological replicates, and error bars represent the SEM, with individual data points overlaid. *P*-values are compared to CK using a two-sided Student's *t*-test. Asterisks (**, and ***) indicate statistical significance at $p < 0.01$ and $p < 0.001$, respectively. The exact *P*-values and source data are provided in the Source Data File.

comparison in Dali server[21] suggested that EfAvs5's NOD is most similar to the plant NLR RPP1(PDB ID: 7CRC, rmsd of 1.160 Å for 56 aligned Cα atoms) and cell death protein 4 in *Caenorhabditis elegans* (PDB ID: 4M9S, rmsd of 1.239 Å for 45 aligned Cα atoms). Notably, we found that EfAvs5 is an inactive ATPase either in the monomer or filament bundle (Fig. 5c). The cryo-EM map allows modeling of an ATP molecule in each NOD active site (Fig. 5d), although we did not add additional ATP during the sample preparation. In the structure, ATP molecules are buried in the active pocket between NBD and WHD (Fig. 5e), with an adjacent magnesium ion coordinated by the canonical Walker A and B motif (Fig. 5f). The K379 and S380 in Walker A form hydrogen bonds with the oxygens of the phosphate groups. Meanwhile, the acidic D426 in Walker B binds to the Mg^{2+}. The recognition of the γ-phosphate group of ATP in the ZAR1 resistosome and Apaf-1 apoptosome is facilitated by an arginine residue in the conserved 'TT/SR' motif, which is crucial for their activation and preserved as 'TTR' and R453 in EfAvs5[22,23]. The I351 forms hydrogen bonds with the N6 atoms of the adenine ring (Fig. 5f). The region spanning residues 300-366, sometimes described as the fish-specific NACHT-associated (FISNA) domain, resembles the active state of NLRP3 (PDB ID:8EJ4)[24]. The accurate positioning of ATP is crucial for the functionality of the EfAvs5 system, as evidenced by the phage plaque assays with WalkerA/B mutants (Fig. 1a). The deficiency of ATP hydrolysis probably results from its WHD domain's unique conformations near the active site, particularly the hydrogen bonding between R537 and the ATP phosphate, contrasting with other active STAND ATPases (Fig. 5f and Supplementary Fig. 13).

To investigate the effect of ATP on the NADase activity of EfAvs5, we conducted standard kinetic assays. The results showed that increasing ATP concentration did not alter EfAvs5's Michaelis constant (K_m) but significantly decreased the maximum reaction velocity (V_{max}), indicating non-competitive inhibition of EfAvs5's NADase activity by ATP ($K_i = 1.74 \pm 0.098$ mM) (Supplementary Fig. 14). We then measured the intracellular ATP concentration of *E. coli* (Supplementary Fig. 15). ATP levels remained ~4 mM during exponential growth, irrespective of EfAvs5 expression. Upon phage infection, ATP concentration in cells expressing EfAvs5 significantly dropped to ~2.3 mM within 10 minutes and further decreased to ~1.5 mM by 60 minutes. ATP levels remained stable in cells lacking EfAvs5. ATP levels naturally decline in non-infected *E. coli* entering stationary phase, aligning with prior studies[25]. Notably, GTP and dGTP also effectively inhibited NADase activity, while other NTPs and dNTPs showed minimal effects, except for a slight inhibition by UTP (Fig. 5g). These results indicate that specific NTP/dNTP can inhibit EfAvs5's NADase activities.

Filament bundle formation mediates EfAvs5 anti-phage activity

EfAvs5 filaments are organized into bundles (Fig. 2a). Interactions between filaments were clearly observed during 2D classification in cryo-EM analysis (Fig. 6a), and the final map of a four-filament bundle was refined to a nominal resolution of 4.3 Å. Focused refinements were conducted on the adjacent filament 2, 3, or 4, yielding resolutions of 4.32 Å, 6.14 Å, and 5.86 Å, respectively (Supplementary Fig. 16 and Supplementary Table 1). EfAvs5 exhibits a head-to-tail contact between dimers from adjacent filaments (Fig. 6b). Notably, the C-terminal sensor possesses a predominantly positive charge, which complements the negatively charged interface of the N-terminal SIR2 domain in adjacent filaments (Fig. 6c). These interactions enable EfAvs5 filament to extend in distinct directions, thereby promoting the

https://doi.org/10.1038/s41467-025-57732-7

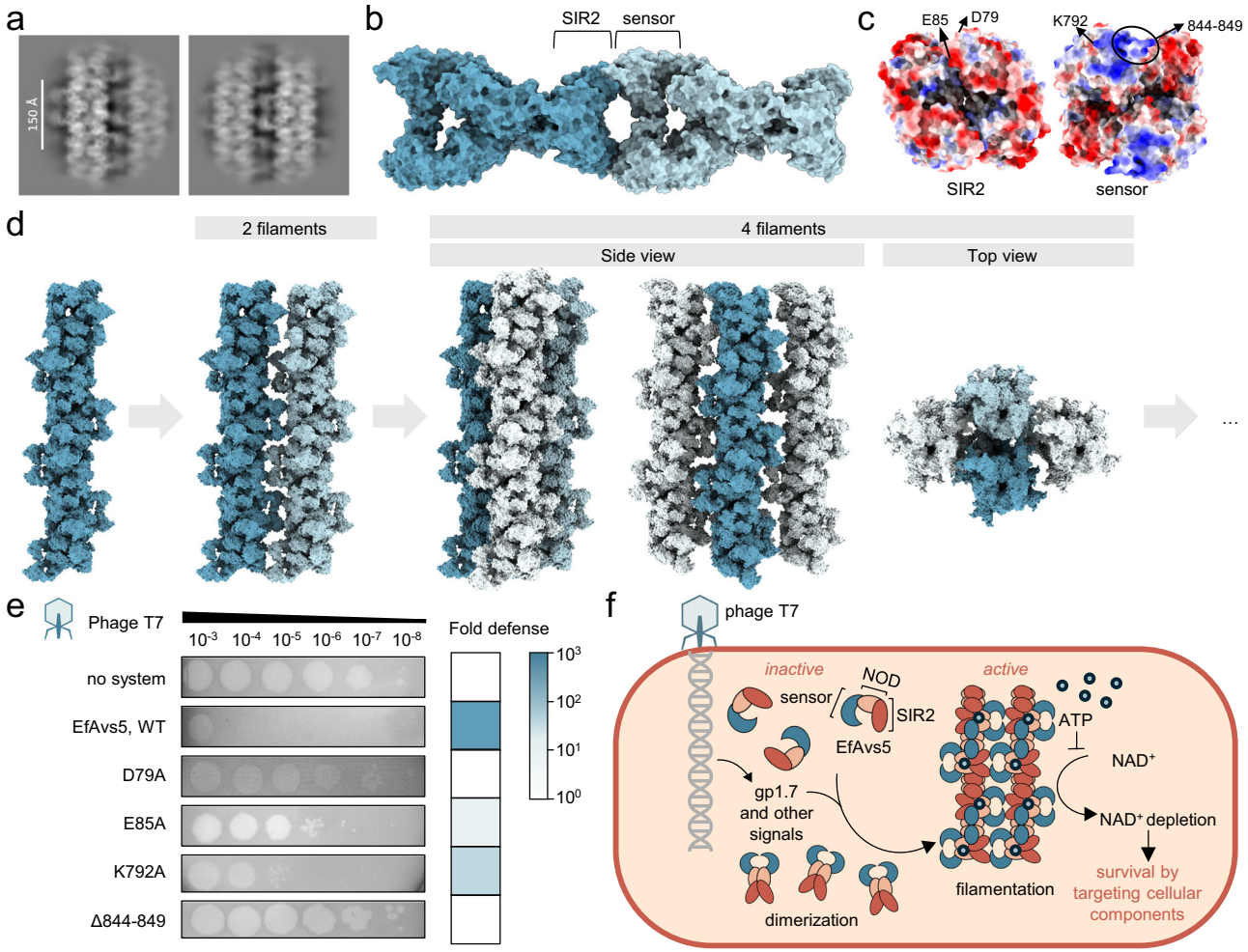

Fig. 6 | Filament bundle formation mediates EfAvs5 anti-phage activity. **a** Representative 2D class averages showing the bundled filament assembly. The scale bar represents 150 Å. **b** Interacting EfAvs5 dimers in adjacent filaments. **c** The electrostatic potential interface of C-terminal sensor and N-terminal SIR2 domain. **d** A schematic diagram of the filament bundle assembly of EfAvs5. **e** Phage plaque assay of *E. coli* expressing EfAvs5 variants with mutations at the bundling interfaces. Data are representative images of $n = 3$ biological replicates. **f** Proposed model of EfAvs5 immune mechanism. Without phage infection, EfAvs5 remains inactive as a monomer. Phage infection activates EfAvs5, forming filament bundles where SIR2 enables survival by targeting cellular components NAD^+. Source data are provided as a Source Data file.

formation of parallel bundles (Fig. 6d). Deletion of the entire C-terminal sensor abolished EfAvs5 activity (Fig. 1a). Further analysis confirmed that deletion of six positively charged amino acids at the C-terminus (Δ844–849) similarly abolished EfAvs5's resistance to phage invasion, as well as the mutations of D79A, E85A and K792A at interaction interfaces (Fig. 6e). The purified E85A mutant exhibited significant turbidity and NADase activity in vitro, whereas no NADase activity was observed for the other mutants (Supplementary Fig. 9). Interestingly, Δ844–849 forms single filament that lacks NADase activity (Supplementary Fig. 17). These results indicate that filament bundle formation is essential for the anti-phage function of EfAvs5.

EfAvs5 is activated by gp1.7 protein of phage T7

Escape mutants are widely used to determine how phages activate defense systems. But we were unable to isolate spontaneous T7 mutants that evaded EfAvs5. Avs proteins have been shown to sense phage large terminases and portal proteins and become toxic when co-expressed with these phage proteins[7]. However, co-expression of T7 large terminase (p57) or portal protein (p42) with EfAvs5 doesn't cause growth inhibition (Supplementary Fig. 18). We then infected cells expressing a FLAG-tagged EfAvs5 with phage T7, and immunoprecipitated the tagged EfAvs5 together with proteins bound to it. Mass spectrometry analysis showed 17 proteins of phage T7 were pulled down together with EfAvs5 (Supplementary Table 2). To test whether EfAvs5 becomes toxic in the presence of these phage T7 proteins, we introduced plasmids carrying the corresponding T7 gene into cells expressing EfAvs5, as well as control cells that did not express EfAvs5 (Supplementary Fig. 18a). With the exception of p16, the expression of these T7 genes alone did not cause significant growth inhibition (Supplementary Fig. 18b). Co-expression of p16 with EfAvs5 resulted in growth inhibition similar to that observed when p16 was expressed alone (Supplementary Fig. 18c). Among the remaining 16 phage T7 proteins, the co-expression of p14 (also known as gp1.7) with EfAvs5 induced the most pronounced growth inhibition, suggesting that gp1.7 protein may be an activator of EfAvs5. Additionally, growth inhibition of gp1.7 and EfAvs5 co-expression is eliminated when the C-terminal sensor of EfAvs5 is removed (Supplementary Fig. 18d). The gp1.7 protein is a nucleotide kinase that phosphorylates dTMP and dGMP to form dTDP and dGDP, presumably maintaining the essential balance of dNTPs[26]. If gp1.7 activates EfAvs5, EfAvs5 would be expected to assemble into filaments when they were co-expressed. The test systems were the same as the liquid culture growth toxicity assays, where only co-expression of both the EfAvs5 and gp1.7 can cause toxicity. Indeed, the lysate precipitate from the co-expression cultures showed significant NADase activity and contained many filament bundles upon negative staining (Supplementary Fig. 19). However, when EfAvs5 or

gp1.7 was expressed alone, only weak NADase activity was detected in the lysate precipitate, and no filaments were observed. These results suggest that T7 gp1.7 may promote the filamentation of EfAvs5 and activate its NADase activity.

Discussion

In this study, we determined cryo-EM structures of EfAvs5 and found that EfAvs5 assembles into filament bundles for NADase activity and anti-phage defense. We propose the following model for EfAvs5 (Fig. 6f). Without phage infection, EfAvs5 adopts an inactive, monomeric conformation in cells. Phage infection, likely the expression of gp1.7, triggers EfAvs5 to form filament bundles, in which SIR2 adopts a dimeric active state. This active state enables EfAvs5 to rapidly degrade NAD^+, targeting cellular components to ensure survival, which ultimately prevents the phage from propagating through a population of cells.

The EfAvs5 structure displays a filament assembly distinct from the characterized SIR2-containing defense systems and STAND proteins. The EfAvs5 filament is formed by EfAvs5 dimers with a C_2 symmetry arranged into a high-order complex, involving comprehensive SIR2-SIR2 and NBD-WHD interactions. In SIR2-APAZ/Ago, DSR2, SIR2-HerA and Thoeris system, SIR2 domains function as monomers, tetramers (dimer of dimers), dodecamers (hexamer of dimers) and filament (spiral of tetramers), respectively[8,9,11,19]. Compared with the SIR2-based filamentation in ThsA, the NOD and SIR2 domain work together to facilitate filament formation in EfAvs5. The activation of STAND family proteins typically involves oligomerization, which includes tetramers (*Se*Avs3, *Ec*Avs4, and plant TIR-NLRs), pentamers (plant ZAR1), heptamers (animal apoptosome Apaf-1) or octamers (Drosophila dark apoptosome)[7,22,23,27,28]. Notably, *Solanum lycopersicum* NRC2 (*Sl*NRC2) was recently found to form filaments at elevated concentrations, but adopt an inactive conformation to avoid self-activation. Distinct from EfAvs5, the *Sl*NRC2 filament consists of three identical protofilaments, which contain copies of tetramers[29]. Despite studies highlighting filamentation's key role in both eukaryotic and prokaryotic immune systems[30,31], EfAvs5's unique filament bundling and its functional significance further underscore the universality and diversity of filamentation as an antiviral mechanism.

The activation observed in our structure appears to be correlated with the high concentration of EfAvs5 proteins, mirroring previous findings in other bacterial immunity systems like Thoeris, Septu and multiple CD-NTases[9,32,33]. In both eukaryotes and prokaryotes, pattern recognition receptors are known to respond to one or more pathogen-associated molecular patterns (PAMPs)[34–36]. Through co-immunoprecipitation and cell toxicity assays, we found that the phage-derived gp1.7 protein is a potential PAMP of EfAvs5, which is capable of inducing EfAvs5 to form filaments and exhibit NADase activity. Homologous proteins to gp1.7 are ubiquitous in *Klebsiella*, *Escherichia*, and *Salmonella* phages, but not in their hosts, potentially underlying the broad resistance conferred by EfAvs5[14]. Here we expand the diversification of molecular pattern recognition in bacterial Avs, yet additional research is required to elucidate the detailed molecular role of gp1.7 in activating EfAvs5 and to determine whether EfAvs5 can recognize other signals. Additionally, we found that ATP plays a complex role in modulating EfAvs5 activity. ATP binding is indispensable for EfAvs5 to defend against phages, yet it lacks ATPase activity. Meanwhile, ATP non-competitively inhibits the NADase activity of EfAvs5. The molecular mechanisms responsible for these observations require further investigation.

Above all, our structural and biochemical findings offer insights into the molecular mechanism of the Avs5 bacterial immune system, particularly regarding how it is activated by phage infection and exerts NADase activity through filamentation.

Methods

Plasmid construction

DNA fragments encoding EfAvs5 from *Escherichia fergusonii* PICI EfCIRHB19-C05 (QML19490.1) were synthesized and inserted into the expressing plasmids pET28a with N-terminal His_6-tag by Universe Gene Technology (Tianjin). The DNA fragment encoding EfAvs5 was subcloned into the pBAD33 vector for phage infection assays. The DNA fragment encoding EfAvs5 was subcloned into the pTAC28 vector for growth toxicity assays. The pTAC28 vector was derived from pET28a through modification, involving the substitution of the T7 promoter with the tac promoter (TTGACAATTAATCATCGGCTCGTATAATG). DNA fragments encoding phage genes were cloned from the genome of phage T7 and inserted into the pBAD33 vector for growth toxicity assays. The phage T7 was obtained from the China Center for Type Culture Collection (CCTCC). Plasmids carrying EfAvs5 mutants were constructed using site-directed mutagenesis. Primers used are listed in Supplementary Table 3.

Protein expression and purification

The vector pET28a-EfAvs5 was transformed into *E. coli* BL21(DE3). Induction of expression was achieved by adding 0.3 mM isopropyl-β-D-thiogalactopyranoside (IPTG) and incubated for 16 h at 16 °C and 220 rpm. The cells were then harvested and resuspended in buffer A (50 mM Tris, pH 8.0, 500 mM NaCl, 5 mM $MgCl_2$, 10% glycerol, 1 mM β-mercaptoethanol and 5 mM imidazole). After purification by nickel-NTA (Smart-Lifesciences), the eluate was further loaded onto a size exclusion chromatography column (SEC) (Superose 6, Cytiva) equilibrated with buffer B (20 mM Tris, pH 8.0, 150 mM NaCl, 5 mM $MgCl_2$, 5% glycerol) and the purified proteins were stored at −80 °C.

Plaque assays

E. coli MG1655 possessing pBAD33- EfAvs5, its mutants or an empty vector(pBAD33) were grown at 37 °C in LB medium. When the OD_{600} reached 0.4, cells were induced with 0.5% L-arabinose (Aladdin, A106195) for 1 hour. Subsequently, 150 μL of the culture was mixed with 3 mL LB medium containing 0.8% low-melting agarose, with 0.5% L-arabinose added. The mixture was then poured onto the LB agar base layer in a 9 cm petri dish. Ten-fold dilutions of high-titers (>10^8 PFU/mL) of phage T7 were spotted onto the agar and incubated overnight at 37 °C. The next day, plates were photographed with blue-white light reflection in the dark box.

Phage-infection in liquid medium

E. coli MG1655 possessing pBAD33- EfAvs5, its mutant(N141A) or an empty vector(pBAD33) were grown until the OD_{600} reached 0.4. These cultures were then induced with 0.5% L-arabinose for 1 hour and diluted in LB containing 0.5% L-arabinose to an OD_{600} of ~0.1. Phage T7 was added to the culture at final MOI of 0.02, 0.2, 2, and 10. Subsequently, 200 μL of the diluted culture was transferred into a 96-well plate. During shaking, the OD_{600} was measured every 5 minutes at 37 °C for 6 hours.

Measurement of colony-forming unit during infection

Overnight cultures of *E. coli* MG1655, either containing the plasmid pBAD33-EfAvs5 or an empty vector, were diluted 1:100 into fresh LB medium. These cultures were grown at 37 °C with the addition of 0.5% L-arabinose until they reached an OD_{600} of 0.4. Subsequently, the cells were harvested by centrifugation, washed with LB, and resuspended to an OD_{600} of 0.2. Phage T7 was added at an MOI of 2 or 5, while control samples were left without phage addition. High MOI was selected to ensure that nearly every cell was infected. Following a 20-minute adsorption period, serial 10-fold dilutions of each sample were plated onto LB agar, and the plates were incubated overnight at 37 °C. The cell survival rate was determined by comparing the colony-forming units (CFU) obtained from the

infected samples to those from the uninfected control samples, and expressed as a percentage.

Phage burst size measurements

Overnight cultures of *E. coli* MG1655 harboring either the pBAD33-EfAvs5 plasmid or an empty vector were diluted 1:100 in LB medium supplemented with 0.5% L-arabinose. These diluted cultures were then grown at 37 °C until they reached an OD_{600} of 0.4. Subsequently, phage T7 was introduced to the cultures at an MOI of 0.1, and the infection process was allowed to proceed at 37 °C. Low MOI was used, as is typically recommended for burst size assays initiated with a lower inoculum. To establish a baseline for the initial phage titer, an equal volume of phage was added to LB media and used as the reference for time 0 of infection. After infection for 20, 40, and 60 minutes at 37 °C, which represent approximately one, two, and three cycles of phage T7 replication, respectively, 0.5 mL samples of the culture were withdrawn. These samples were centrifuged at 5000 × *g* for 7 minutes and the supernatants were filtered through a 0.22 μm filter. The titer of the phages present in the filtered supernatants was determined by a plaque assay using *E. coli* MG1655 as the host.

Live/dead staining

Cultures of *E. coli* MG1655 harboring either the pBAD33-EfAvs5 plasmid or an empty vector were grown in LB medium to an OD_{600} of 0.4, and infected with phage T7 at an MOI of 2. At indicated times, 1 mL cultures were centrifuged at 10,000 × *g* for 5 min, washed with physiological saline, and adjusted to ~10^6 bacteria/ml and stained with a viability dye (DMAO and PI, Beyotime, C2030S) in a 96-well plate. DMAO (N,N-dimethylaniline N-oxide) is a green fluorescent dye for nucleic acids with membrane permeability, capable of staining both viable and non-viable cells. In contrast, PI is a non-permeable fluorescent dye that can only penetrate dead bacteria with compromised membrane integrity, where it forms PI-DNA complexes that emit red fluorescence. After incubation at 37 °C for 15 min, relative fluorescence units (RFU) were measured using the BioTek Synergy H1 microplate reader at specific excitation/emission wavelengths for DMAO (503/530 nm) and PI (535/617 nm). To establish a standard curve for bacterial viability, separate aliquots of bacteria were treated with physiological saline (live bacteria) or a 7:3 mixture of ethanol/isopropanol and saline (dead bacteria), incubated for 1 h, washed, and resuspended to ~10^6 bacteria/ml. Live and dead bacteria were mixed at different ratio in 96-well plates to generate standards for staining and RFU measurement.

NAD(H) degradation measurements

NAD(H) concentrations were measured using the Innochem Coenzyme I NAD(H) Content Assay Kit (WST colorimetry, BC5190), following the manufacturer's instructions. Briefly, overnight cultures were diluted 1:100 in 50 mL LB with 0.5% L-arabinose, grown to OD_{600} of 0.4, and infected with phage T7 at an MOI of 2. An MOI of 2 was selected to ensure sustained bacterial growth during the expression of the EfAvs5 system, thereby enabling the accurate quantification of NAD^+ content. At indicated times, 1 mL cultures were centrifuged, resuspended in acidic extract, sonicated, boiled, rapid cooled, and centrifuged. The supernatant was neutralized with an alkaline extract. 50 μL of the neutralized supernatant was combined sequentially with 250 μL of Reagent 1, 75 μL of Reagent 2, 150 μL of Reagent 3, and 35 μL of Reagent 4 in the determination tube. After a 1-hour dark reaction, Reagent 5 was added to the mixture. In the control tube, Reagent 5 was added first, followed by the supernatant, maintaining identical steps thereafter. Absorbance was measured at 450 nm, and NAD(H) levels were calculated using a standard curve and normalized to the amount of NAD(H) present in an equivalent volume of sample with an OD_{600} of 0.1 to allow for accurate comparisons between samples.

Negative staining analysis

The EfAvs5 proteins (approximately 100 ng/μL) was directly applied to a glow-discharged 400-mesh Cu grid (Beijing ZhongJingKeYi Technology) for 30 s. After side blotting, the grid was immediately stained with 2% uranyl formate and then blotted again from the side. Staining was repeated twice with a 30 s incubation with uranyl formate in the final staining step. EM images were collected on a Talos F200C G2 at a nominal magnification of 57,000× or 72,000×, and at a defocus of about 5 μm.

Turbidity assay

The freshly purified EfAvs5 proteins or their mutant variants were diluted or concentrated to varying concentrations. The high purity of the proteins was confirmed through SDS-PAGE analysis followed by Coomassie blue R250 staining. The samples were then aliquoted and stored at −80 °C. After different durations, their OD_{330} were measured using a micro spectrophotometer (Nanodrop, Thermo Scientific). All experiments were conducted in triplicate to ensure reproducibility.

Dynamic light scattering

Dynamic light scattering measurements were conducted using the DynaPro NanoStar II instrument from Wyatt. EfAvs5 at a concentration of 20 μM was stored in a buffer comprising 20 mM Tris, pH 8.0, 150 mM NaCl, 5 mM $MgCl_2$, and 5% glycerol. 100 μl of the sample was loaded into a cuvette. The measurements took place at 25 °C with an acquisition time of 5 seconds. The cumulant method was employed for fitting and calculation, and the data showed the intensity-based content of each component based on scattered light. Data represent the calculated average from five separate measurements.

Cryo-EM grid preparation and data acquisition

3.5 μL of the EfAvs5 samples were added to freshly glow-discharged Quantifoil R1.2/1.3 Cu 300 mesh grids. In a Vitrobot (FEI, Inc.), grids were plunge-frozen in liquid ethane after being blotted for 2 s at 16 °C with 100% chamber humidity. The grids were imaged using EPU on Titan Krios 300 kV microscopes with a K3 detector. A total of 4318 movies were collected under the defocus ranging from −0.8 to −1.6 μm, and the magnification was 81k in super-resolution mode. 32 frames per movie were collected with a total dose of 40 $e^-/Å^2$.

Cryo-EM data processing and model building

The cryo-EM data was processed using CryoSPARC suite v4.5.3[37]. After motion correction, patch CTF estimation and manual exposure curation, 1425 movies were selected. The first set of particles was picked using a filament tracer, and after two-dimensional (2D) classification, good templates were selected for template picking. A total of 1,392,237 particles were picked using a template picker and extracted (box size 360 pixels) from 1425 accepted micrographs (Supplementary Fig. 4). Two rounds of 2D classification were conducted, and 364,551 particles were picked and used for ab-initio reconstruction (three classes). The largest 3D class (228,053 particles, 62.6%) was selected and refined by homogeneous refinement, non-uniform refinement and CTF refinement to give the final map (global resolution, 3.44 Å). Helical parameters (helical twist and helical rise) were determined by helical refinement job. The initial model of EfAvs5 was generated by AlphaFold[38]. The model of ATP was built in Coot[39]. The models of EfAvs5 were fitted into the cryo-EM density maps using ChimeraX[40]. The model was refined in Coot and Phenix with secondary structure, rotamer, and Ramachandran restraints[41]. The Map versus Model FSCs were generated by Phenix (Supplementary Fig. 4). The statistics of cryo-EM data processing and refinement were listed in Supplementary Table 1.

For the bundled EfAvs5 analysis, particles utilized for the reconstruction of a single filament (228,053 particles) were re-extracted using a box size doubled from the original. Following this, two rounds

of 2D classification were performed, resulting in the selection of 181,548 particles for ab-initio reconstruction. These particles were subsequently downsampled and subjected to homogeneous refinement to produce the final map, which achieved a global resolution of 4.31 Å. The signals from three adjacent filaments weakened during the refinement. Therefore, local refinements were conducted focused on the adjacent filaments 2, 3, and 4 to obtain higher-quality final maps.

In vitro NADase activity

The EfAvs5 NADase activity was evaluated through an εNAD$^+$-based fluorescence assay, wherein the enzymatic cleavage of the nicotinamide glycosidic bond in εNAD$^+$ results in the formation of εADPR, which subsequently emits a fluorescent signal. In a 96-well black flat-bottom plate, 100 µL reaction mixtures were prepared, each containing 50 µM of εNAD$^+$ (Sigma, N2630) and 0.5 µM EfAvs5 proteins in reaction buffer (20 mM Tris, pH 8.0, 150 mM NaCl, and 5% glycerol, with or without the addition of nucleotides). The reactions were then loaded into a BioTek Synergy H1 microplate reader, and fluorescence intensities were recorded at 37 °C every 20 seconds for 15 minutes, employing excitation and emission wavelengths of 310 nm and 410 nm, respectively. All experiments were conducted in triplicate to ensure reproducibility. To better assess the impact of ATP on the NADase activity of Avs5, a standard kinetic analysis was performed. The reaction mixture contained 0.5 µM of Avs5, varying concentrations of NAD$^+$, and increasing concentrations of ATP. For each set of reactions, the initial velocity of the enzymatic reaction was determined. The plots were fitted to the Michaelis-Menten equation using GraphPad Prism 8.0.2 statistical software to estimate the K_m and V_{max} for each condition. The inhibitor patterns were determined based on the changes in K_m and V_{max} across different ATP concentrations. The inhibitory constant (K_i) was calculated using GraphPad Prism 8.0.2 using the non-competitive inhibition model.

Liquid culture growth toxicity assays

Overnight cultures of non-induced *E. coli* MG1655 were prepared, including strains with the pBAD33 carrying the corresponding T7 gene, strains co-transformed with the pBAD33 carrying the corresponding T7 gene and pTAC28-EfAvs5, and strains co-transformed with an empty pBAD33 vector and pTAC28-EfAvs5. These cultures were then diluted to an OD_{600} of 0.2 at 37 °C. The inducers were then added to a final concentration of 0.2% arabinose, and LB was added instead for the uninduced control cells. The leaked expression of Avs5 in cells containing pTAC28-EfAvs5 is sufficient to provide phage resistance and is not cytotoxic. The cultures were transferred into a 96-well plate. Plates were incubated at 37 °C with shaking in the BioTek Synergy H1 microplate reader with an OD_{600} measurement taken every 2.5 min. For the cells containing pET28a carrying wild-type or mutant EfAvs5 gene, the inducers were 0.025 mM IPTG.

ATPase activity

ATPase activities were evaluated by using the Malachite Green Phosphate Detection Kit (Beyotime, S0196S). Each reaction mixture consisted of 5 µM EfAvs5 proteins in a reaction buffer (20 mM Tris, pH 8.0, 150 mM NaCl, 5 mM $MgCl_2$, and 0.5 mM ATP). A mixture without the addition of EfAvs5 proteins served as a control. Following a 30-minute incubation at 37 °C, color reagent was added, and the mixture was further incubated for another 30 minutes. Subsequently, the absorbance at 620 nm was measured using the BioTek Synergy H1 microplate reader. Phosphate levels were then calculated using a standard curve generated with phosphate standards. All experiments were conducted in triplicate to ensure reproducibility.

Measurement of cellular ATP concentrations

The BacTiter-Lumi™ reagent (Beyotime, C0052S) was equilibrated to room temperature. A black 96-well plate was used, with each well adding 100 µl of bacteria (OD_{600} measured) and 100 µl of the reagent. Negative controls were set up with culture medium and the reagent. After mixing and incubating at room temperature for 30 minutes, luminescence was detected using the BioTek Synergy H1 microplate reader (0.5 s/well). ATP content was calculated from a standard curve generated with ATP standards. The intracellular ATP concentration was determined by dividing ATP content by the cell number and assumed cellular volume. In 1 ml *E.coli* cultures with an OD_{600} of 0.5, there are approximately 2×10^8 cells. Additionally, the average volume of each cell is 10^{-15} liters[25,42,43].

Co-immunoprecipitation assay

Overnight cultures of *E. coli* MG1655 expressing FLAG-tagged EfAvs5 were diluted 1:100 in 50 mL LB with 0.5% L-arabinose, grown to OD_{600} of 0.5, and infected with phage T7 at an MOI of 5. After 20 minutes, cultures were centrifuged, resuspended and lysed in RIPA buffer and then centrifuged to 10,000 ×*g* for 10 minutes at 4 °C to remove cellular debris. The 500 µL supernatant was mixed with 10 µL Anti-Flag Magnetic Beads (ShareBio, SB-PR002) overnight at 4 °C with rotation. After 4 washes in PBST (PBS + 1% Triton X-100), beads were resuspended in 50 µL glycine HCl, pH3.0 for 5 minutes. The pH of the eluted samples was neutralized using 1 M Tris at a pH of 8.0. The eluted samples were then stored at −80 °C for further analysis.

Mass Spectrometry analysis

The eluted samples from co-immunoprecipitation assays ($n = 1$) were digested with trypsin (Promega) and analyzed with nano-liquid chromatography-mass spectrometry (nano-LC-MS) system (nanoElute2-Timstof pro2, Bruker, German). Peptide separation used a self-packed analytical PicoFrit column (New Objective, Woburn, MA, USA) (75 µm × 20 cm length) with C18 material of ReproSil-Pur 120 A C18-Q 1.9 µm (Dr. Maisch GmbH, Ammerbuch, Germany). Buffer A was composed of 0.1% formic acid in water, and buffer B was composed of 100% acetonitrile containing 0.1% formic acid. A 1-h gradient with buffer B from 2 to 95% at a flow rate of 300 nL/min was conducted for separation. The acquisition mode is diaPASEF. The MS scanning range is 100–1700, with a DIA window scanning range of 400–1201 m/z. The number of isolation windows is set to 32, and the isolation window width is configured at 26 Da. The cycle time is 1.8 s. During the PASEF MS/MS scanning process, the collision energy increases linearly with ion mobility, ranging from 20 eV (at $1/K_0 = 0.6$ Vs/cm^2) to 59 eV (at $1/K_0 = 1.6$ Vs/cm^2). Data analysis was conducted using Spectronaut v19.1 with default BGS factory settings. Modifications considered were fixed carbamidomethylation (C + 57.02 Da), variable oxidations (M + 15.99 Da), deamidations (NQ), and N-terminal acetylation (+42.011 Da). The software automatically corrected retention times, mass windows, and determined optimal extraction windows. Criteria for protein qualification were set at a 1.0% FDR threshold for both precursors and proteins. The decoy database was generated using a mutated strategy, similar to scrambling amino acid sequences by a random number (minimum of 2 amino acids, maximum of half the total peptide length). Automatic correction was conducted followed by normalization using the signal intensities of all successfully identified parent ions. The MaxLFQ method was employed for the quantification of protein groups. The Q-value corrected by the Benjamini-Hochberg (BH) method was applied to set the confidence threshold.

Phylogenetic analysis of Avs5 systems

The coding sequence of Avs5 was acquired from two sources: firstly, by utilizing the defense finder tool v1.3.0[44] to scan through all bacterial and archaeal genomes housed in the IMG (Integrated Microbial Genomes & Microbiomes) database from November 2023, aiming to identify proteins that encode the Avs5 system; secondly, by leveraging the Foldseek search server to discover proteins (AlphaFold/UniProt50

database, ensuring a coverage exceeding 80%) that exhibited high structural similarity to EfAvs5[45]. To eliminate redundancy, MMseqs was employed with the specified parameters '–min-seq-id 0.90' and '-c 0.8', resulting in 263 filtered sequences[46]. These sequences were subsequently aligned using MAFFT v7.520, with the parameters set to '--maxiterate 1000 –globalpair' for optimal alignment[47]. Following alignment, trimAl was applied to refine the alignment by trimming unnecessary regions[48]. The phylogenetic tree was then constructed using IQ-TREE v2.1.4, incorporating the parameters '-nstop 500 -bb 1000 -m LG + F + I + G4' for enhanced accuracy and robustness[49]. Finally, iTOL was utilized for the visualization and annotation of the phylogenetic tree[50].

Reporting summary

Further information on research design is available in the Nature Portfolio Reporting Summary linked to this article.

Data availability

The atomic coordinates have been deposited in the Protein Data Bank under accession codes 9JAP (EfAvs5 filament structure). The corresponding maps have been deposited in the Electron Microscopy Data Bank under the accession number EMD-61299 (EfAvs5 filament structure), EMD-62763 (Bundled EfAvs5 filament structure), EMD-62759 (Local map of EfAvs5 Filament 2), EMD-62760 (Local map of EfAvs5 Filament 3), EMD-62762 (Local map of EfAvs5 Filament 4). The mass spectrometry proteomics data have been deposited to the ProteomeXchange Consortium via the PRIDE[51] partner repository with the dataset identifier PXD060416. Source data are provided with this paper.

References

1. Millman, A. et al. An expanded arsenal of immune systems that protect bacteria from phages. *Cell Host Microbe* **30**, 1556–1569.e1555 (2022).
2. Vassallo, C. N., Doering, C. R., Littlehale, M. L., Teodoro, G. I. C. & Laub, M. T. A functional selection reveals previously undetected anti-phage defence systems in the E. coli pangenome. *Nat. Microbiol.* **7**, 1568–1579 (2022).
3. Gao, L. et al. Diverse enzymatic activities mediate antiviral immunity in prokaryotes. *Science* **369**, 1077–1084 (2020).
4. Leipe, D. D., Koonin, E. V. & Aravind, L. STAND, a class of P-loop NTPases including animal and plant regulators of programmed cell death: multiple, complex domain architectures, unusual phyletic patterns, and evolution by horizontal gene transfer. *J. Mol. Biol.* **343**, 1–28 (2004).
5. Huang, S. et al. NLR signaling in plants: from resistosomes to second messengers. *Trends Biochem. Sci.* **48**, 776–787 (2023).
6. Mitchell, P. S., Sandstrom, A. & Vance, R. E. The NLRP1 inflammasome: new mechanistic insights and unresolved mysteries. *Curr. Opin. Immunol.* **60**, 37–45 (2019).
7. Gao, L. A. et al. Prokaryotic innate immunity through pattern recognition of conserved viral proteins. *Science* **377**, eabm4096 (2022).
8. Koopal, B. et al. Short prokaryotic Argonaute systems trigger cell death upon detection of invading DNA. *Cell* **185**, 1471–1486.e1419 (2022).
9. Ka, D., Oh, H., Park, E., Kim, J.-H. & Bae, E. Structural and functional evidence of bacterial antiphage protection by Thoeris defense system via NAD+ degradation. *Nat. Commun.* **11**, 2816 (2020).
10. Garb, J. et al. Multiple phage resistance systems inhibit infection via SIR2-dependent NAD+ depletion. *Nat. Microbiol.* **7**, 1849–1856 (2022).
11. Tang, D. et al. Multiple enzymatic activities of a Sir2-HerA system cooperate for anti-phage defense. *Mol. Cell* **83**, 4600–4613.e4606 (2023).
12. Tamulaitiene, G. et al. Activation of Thoeris antiviral system via SIR2 effector filament assembly. *Nature*, **627**, 431–436 (2024).
13. Yang, X., Wang, Y. & Zheng, J. Structural insights into autoinhibition and activation of defense-associated sirtuin protein. *Int. J. Biol. Macromol.* **277**, 134145 (2024).
14. Fillol-Salom, A. et al. Bacteriophages benefit from mobilizing pathogenicity islands encoding immune systems against competitors. *Cell* **185**, 3248–3262.e3220 (2022).
15. Aframian, N. & Eldar, A. Abortive infection antiphage defense systems: separating mechanism and phenotype. *Trends Microbiol.* **31**, 1003–1012 (2023).
16. Morehouse, B. R. et al. Cryo-EM structure of an active bacterial TIR–STING filament complex. *Nature* **608**, 803–807 (2022).
17. Hogrel, G. et al. Cyclic nucleotide-induced helical structure activates a TIR immune effector. *Nature* **608**, 808–812 (2022).
18. Du, J. et al. Sirt5 is a NAD-dependent protein lysine demalonylase and desuccinylase. *Science* **334**, 806–809 (2011).
19. Yin, H. et al. Insights into the modulation of bacterial NADase activity by phage proteins. *Nat. Commun.* **15**, 2692 (2024).
20. Kaur, G., Iyer, L. M., Burroughs, A. M. & Aravind, L. Bacterial death and TRADD-N domains help define novel apoptosis and immunity mechanisms shared by prokaryotes and metazoans. *Elife* **10**, e70394 (2021).
21. Holm, L. Dali server: structural unification of protein families. *Nucleic Acids Res.* **50**, W210–w215 (2022).
22. Wang, J. et al. Reconstitution and structure of a plant NLR resistosome conferring immunity. *Science* **364**, eaav5870 (2019).
23. Zhou, M. et al. Atomic structure of the apoptosome: mechanism of cytochrome c- and dATP-mediated activation of Apaf-1. *Genes Dev.* **29**, 2349–2361 (2015).
24. Xiao, L., Magupalli, V. G. & Wu, H. Cryo-EM structures of the active NLRP3 inflammasome disc. *Nature* **613**, 595–600 (2023).
25. Buckstein, M. H., He, J. & Rubin, H. Characterization of nucleotide pools as a function of physiological state in Escherichia coli. *J. Bacteriol.* **190**, 718–726 (2008).
26. Tran, N. Q., Tabor, S., Amarasiriwardena, C. J., Kulczyk, A. W. & Richardson, C. C. Characterization of a nucleotide kinase encoded by bacteriophage T7. *J. Biol. Chem.* **287**, 29468–29478 (2012).
27. Ma, S. et al. Direct pathogen-induced assembly of an NLR immune receptor complex to form a holoenzyme. *Science* **370**, eabe3069 (2020).
28. Pang, Y. et al. Structure of the apoptosome: mechanistic insights into activation of an initiator caspase from Drosophila. *Genes Dev.* **29**, 277–287 (2015).
29. Ma, S. et al. Oligomerization-mediated autoinhibition and cofactor binding of a plant NLR. *Nature* **632**, 869–876 (2024).
30. Payne, L., Jackson, S. & Pinilla-Redondo, R. Supramolecular assemblies in bacterial immunity: an emerging paradigm. *Trends Microbiol.* **32**, 828–831 (2024).
31. Yin, Q., Fu, T. M., Li, J. & Wu, H. Structural biology of innate immunity. *Annu. Rev. Immunol.* **33**, 393–416 (2015).
32. Whiteley, A. T. et al. Bacterial cGAS-like enzymes synthesize diverse nucleotide signals. *Nature* **567**, 194–199 (2019).
33. Rousset, F. et al. A conserved family of immune effectors cleaves cellular ATP upon viral infection. *Cell* **186**, 3619–3631.e3613 (2023).
34. Pradeu, T., Thomma, B. P. H. J., Girardin, S. E. & Lemaitre, B. The conceptual foundations of innate immunity: Taking stock 30 years later. *Immunity* **57**, 613–631 (2024).
35. Kawai, T. & Akira, S. The roles of TLRs, RLRs and NLRs in pathogen recognition. *Int. Immunol.* **21**, 317–337 (2009).
36. Kibby, E. M. et al. A bacterial NLR-related protein recognizes multiple unrelated phage triggers to sense infection. *bioRxiv*, https://doi.org/10.1101/2024.12.17.629029 (2024).

37. Punjani, A., Rubinstein, J. L., Fleet, D. J. & Brubaker, M. A. cryoSPARC: algorithms for rapid unsupervised cryo-EM structure determination. *Nat. Methods* **14**, 290–296 (2017).
38. Jumper, J. et al. Highly accurate protein structure prediction with AlphaFold. *Nature* **596**, 583–589 (2021).
39. Casanal, A., Lohkamp, B. & Emsley, P. Current developments in Coot for macromolecular model building of Electron Cryo-microscopy and Crystallographic Data. *Protein Sci.* **29**, 1069–1078 (2020).
40. Pettersen, E. F. et al. UCSF ChimeraX: Structure visualization for researchers, educators, and developers. *Protein Sci.* **30**, 70–82 (2021).
41. Liebschner, D. et al. Macromolecular structure determination using X-rays, neutrons and electrons: recent developments in Phenix. *Acta Crystallogr. D. Struct. Biol.* **75**, 861–877 (2019).
42. Kubitschek, H. E. & Friske, J. A. Determination of bacterial cell volume with the Coulter Counter. *J. Bacteriol.* **168**, 1466–1467 (1986).
43. Bremer, H. & Dennis P. P. Modulation of chemical composition and other parameters of the cell at different exponential growth rates. *EcoSal Plus* **3**, https://doi.org/10.1128/ecosal.5.2.3 (2008).
44. Tesson, F. et al. Systematic and quantitative view of the antiviral arsenal of prokaryotes. *Nat. Commun.* **13**, 2561 (2022).
45. van Kempen, M. et al. Fast and accurate protein structure search with Foldseek. *Nat. Biotechnol.* **42**, 243–246 (2024).
46. Steinegger, M. & Söding, J. MMseqs2 enables sensitive protein sequence searching for the analysis of massive data sets. *Nat. Biotechnol.* **35**, 1026–1028 (2017).
47. Katoh, K., Rozewicki, J. & Yamada, K. D. MAFFT online service: multiple sequence alignment, interactive sequence choice and visualization. *Brief. Bioinform.* **20**, 1160–1166 (2019).
48. Capella-Gutiérrez, S., Silla-Martínez, J. M. & Gabaldón, T. trimAl: a tool for automated alignment trimming in large-scale phylogenetic analyses. *Bioinformatics* **25**, 1972–1973 (2009).
49. Nguyen, L. T., Schmidt, H. A., von Haeseler, A. & Minh, B. Q. IQ-TREE: a fast and effective stochastic algorithm for estimating maximum-likelihood phylogenies. *Mol. Biol. Evol.* **32**, 268–274 (2015).
50. Letunic, I. & Bork, P. Interactive Tree Of Life (iTOL) v5: an online tool for phylogenetic tree display and annotation. *Nucleic Acids Res.* **49**, W293–w296 (2021).
51. Perez-Riverol, Y. et al. The PRIDE database at 20 years: 2025 update. *Nucleic Acids Res.* **53**, D543–d553 (2025).

Acknowledgements

This work was supported by National Key Research and Development Program of China (grant no. 2020YFA0907900 to J.Z.) and National Natural Science Foundation of China (grant no. 32370071, 32070040 to J.Z.). We thank the staff members of the Electron Microscopy System at the National Facility for Protein Science in Shanghai (https://cstr.cn/31129.02.NFPS), for providing technical support and assistance in data collection and analysis. We thank Jing Liu, Xinqiu Guo, Mengyu Yan, Jingli Hou and Zheng Jin at the Instrument Analysis Center (IAC) of Shanghai Jiao Tong University for providing assistance in data collection and mass spectrometry analysis. The vector pTAC28 was generously provided by Professor Delin You.

Author contributions

J.Z. and Y.W. designed the experiments and analyzed the data. Y.W. and Y.T. performed biochemical assays. Y.W. and X.Y. conducted cryo-EM data collection. Y.W. conducted image processing, atomic model, building and refinement, and structural analyses. Y.W. and F.Y. performed bioinformatics analysis. Y.W. and J.Z. wrote the manuscript.

Competing interests

The authors declare no competing interests.

Additional information

Supplementary information The online version contains supplementary material available at https://doi.org/10.1038/s41467-025-57732-7.

Correspondence and requests for materials should be addressed to Jianting Zheng.

Peer review information *Nature Communications* thanks Jack Bravo, Malcolm White, and the other anonymous reviewer(s) for their contribution to the peer review of this work. A peer review file is available.